

New insights in laser-generated ultra-intense γ -ray and neutron sources for nuclear application and science

M. M. Günther,^{1,*} O. N. Rosmej,^{1,2,3} P. Tavana,² M. Gyrdaymov,² A. Skobliakov,⁴
A. Kantsyrev,⁴ S. Zähler,^{1,2} N. G. Borisenko,⁵ A. Pukhov,⁶ and N. E. Andreev^{7,8}

¹*GSI-Helmholtzzentrum für Schwerionenforschung GmbH, Planckstraße 1, 64291 Darmstadt, Germany*

²*Goethe-Universität Frankfurt am Main, Max-von-Laue-Str.1, 60438 Frankfurt am Main, Germany*

³*Helmholtz Forschungsakademie Hessen für FAIR (HFHF), Campus Frankfurt am Main, Germany*

⁴*Institute for Theoretical and Experimental Physics named by A.I. Alikhanov of NRC «Kurchatov Institute»,
B. Cheremushkinskaya 25, 117218 Moscow, Russia*

⁵*P. N. Lebedev Physical Institute, RAS, Leninsky Prospekt 53, 119991 Moscow, Russia*

⁶*Heinrich-Heine-Universität Düsseldorf, Universitätsstraße 1,
Gebäude 25.32 Etage 01, 40225 Düsseldorf, Germany*

⁷*Joint Institute for High Temperatures, RAS, Izhorskaya st. 13, Bldg. 2, 125412 Moscow, Russia*

⁸*Moscow Institute of Physics and Technology (State University),
Institutskiy Pereulok 9, 141700 Dolgoprudny Moscow region, Russia*

Ultra-intense MeV photon and neutron beams are indispensable tools in many research fields such as nuclear, atomic and material science as well as in medical and biophysical applications. For astrophysical applications aimed for laboratory investigations, neutron fluxes in excess of 10^{21} n/(cm² s) are required. Such ultra-high fluxes are unattainable with existing conventional reactor- and accelerator-based facilities. Currently discussed concepts for generating high-flux neutron beams are based on ultra-high-power multi-petawatt lasers operating at $>10^{23}$ W/cm² intensities. Here, we present a novel efficient concept for generating γ and neutron beams based on enhanced generation of direct laser accelerated electrons in relativistic laser interactions with a long-scale near critical density plasma at 10^{19} W/cm² intensity. New experimental insights in the laser-driven generation of ultra-intense well-directed multi-MeV beams of photons with $>10^{12}$ ph/sr and a ultra-high intense neutron source with $>6 \times 10^{10}$ neutrons per shot are presented. More than 1.4% laser-to-gamma conversion efficiency above 10 MeV and 0.05% laser-to-neutron conversion efficiency were recorded, already at moderate relativistic laser intensities and ps pulse duration. This approach promises a strong boost of the diagnostic potential of existing kJ PW laser systems used for ICF research.

I. INTRODUCTION

Ultra-intense γ and neutron beams are of immense interest in laboratory astrophysics, high energy density plasma physics [1–6] and applications e.g. in biology, medicine and material science [7–14].

High-brilliant γ beams open new possibilities for selective excitation of atomic nucleus states for investigation of photo-disintegration reactions in nuclear astrophysics [15] as well as for applications in the efficient production of medical radioisotopes for diagnostics and radiooncological therapeutics, such as scandium, copper and platinum isotopes [11, 12, 16–18]. Also, studies of nuclear resonance fluorescence (NRF) processes of strong excitation states in nuclei are attractive for the development of isotope selective radiographic imaging techniques [19].

Neutron sources are indispensable tools for approving astrophysical nucleosynthesis theories, where the production of bulk heavy nuclei beyond iron (Fe) is attributed to the slow (s) and rapid (r) neutron capture processes. Nuclear reaction cross sections for nuclear structure physics studies can be accessed by means of conventional neutron sources based on electron accelerators [20], nuclear

fission reactors like high-flux neutron reactor of the Institut Laue-Langevin (ILL) [21], and spallation sources [22]. The ILL reactor (10^{15} n/(cm² s)) [21] and the upcoming European Spallation Source (ESS) with $>10^{16}$ n/(cm² s) [23] are examples for the highest peak-fluxes of existing neutron sources. For most applications, especially in nuclear astrophysics, the fast neutrons have to be moderated to the epithermal neutron energy range which decreases the effective neutron flux on the target. For nuclear astrophysical studies the so-called Time-Of-Flight (TOF) facilities are preferable to reach suitable conditions for neutron energy distribution. For example the LANSCE facility of the Los Alamos National Laboratory in the USA provides neutron peak-fluxes of $>10^{15}$ n/(cm² s) as well as an integrated neutron flux of $>10^5$ n/(cm² s) in the nuclear astrophysical relevant neutron energy range between 10 – 100 keV [24]. Currently, quasi-stellar beam conditions for nuclear astrophysical investigations provides the *Frankfurt Neutron Source of the Stern Gerlach Zentrum* (FRANZ) with an integrated neutron flux of 6×10^6 n/(cm² s) in the energy range of 10 – 100 keV on target [13, 25].

Investigation of the r-process for nucleosynthesis of heavy isotopes takes place along the chain of short-lived isotopes where the neutron capture time is shorter than the time of the β^- -decay [13, 26]. For r-process studies, nuclear quantities such as β -decay properties, masses and

* m.guenther@gsi.de

neutron capture rates for nuclei far from the so-called *valley of stability* are of key importance and are still an experimental challenge [27]. One example for a suitable initial isotope for the investigation of multi-neutron capture events in the r-process chain, but also in the s-process scheme is the stable ^{96}Zr isotope [28, 29]. Chen et al. [29] have shown in simulations that for multiple neutron capture processes, a neutron peak-flux of 10^{24} n/(cm² s) is required to ensure the neutron capture time (≈ 1 s) shorter than the $^{97-102}\text{Zr}$ isotope half-lives. The neutron capture time is determined by the product of the neutron peak-flux and the capture cross section. Therefore, especially for laboratory nuclear astrophysical studies the development of neutron sources with high neutron-fluxes and neutron energies from tenth of keV to several hundreds of keV are of great importance. Recent theoretical studies of the neutron capture cascade using laser-driven neutron sources have shown the feasibility for neutron capture nucleosynthesis in the laboratory [30].

An alternative way for the generation of high-fluence and high-flux γ and neutron beams in compact facilities is based on high-power lasers in relativistic laser-plasma interactions. Upcoming high-brilliance and high-intensity γ beam facilities like the Variable-Energy Gamma Ray system (VEGA) at ELI-NP will produce tunable and narrow γ beams via Compton backscattering of 100 TW laser pulses on relativistic electrons with energies above 700 MeV [9]. The planned upgrade of the high intense γ -ray source, HI γ S-2, will provide up to 20 MeV γ beams via Compton backscattering in a conventional accelerator based free electron laser (FEL) structure [31]. Also in construction is the Gamma Factory facility at CERN that provides γ beams with energies of several hundreds of MeV generated via the excitation of highly ionized relativistic heavy ions by lasers [10]. Such facilities allow for a renaissance in photo-nuclear research field. A review to a prospective possible pathway to reach peak neutron-fluxes of $10^{21}-10^{24}$ n/(cm² s) applicable for investigating nucleosynthesis in the laboratory is reported using ultra-high power (multi-PW) lasers with intensities up to $>10^{23}$ W/cm² [29].

In general, two principal laser-plasma based methods are being pursued to generate γ beams in the MeV regime. On the one hand we consider the electron acceleration via the laser-driven plasma wake field based on the relativistic laser pulse interaction with a gas target (under dense plasma) at several tens of femtosecond pulse duration [32]. The interaction of the GeV quasi mono-energetic electrons with the contra-propagating laser pulse [33, 34] leads to the generation of narrow band beams of Compton backscattered photons [35] with energies at γ_e^2 of the laser photon energy, where $\gamma_e = \frac{1}{\sqrt{1-(\frac{v_e}{c})^2}}$ is the electron Lorentz factor. On the other hand by interaction of relativistic laser pulses with high- Z solid targets, electrons can be ponderomotively accelerated in the low-dense pre-plasma region in front of the target [36, 37]. Relativistic electrons are then decelerated in a high- Z sample producing continuous MeV-

bremstrahlung radiation [38–40]. New concepts for producing multi-MeV highly brilliant photon beams from MeV-betatron emission of trapped GeV-electrons were theoretically discussed for the next generation of ultra-high intense lasers [41–44]. Such new single laser schemes allow to investigate of quantum electrodynamic (QED) effects and QED plasmas [43, 44]. Additionally, simulation studies considering a counter propagating multi-PW laser scheme for two-side irradiation have shown promising results in the production of enhanced electron-positron plasma density for strong-field QED investigations [45].

Currently, besides neutron generation in inertial fusion processes [5, 6], there are several other scenarios for the laser-based production of neutrons via nuclear reactions: Accelerated deuterons interact with heavy or light isotopes resulting in compound nucleus excitations or direct reactions. In the latter case, neutrons with energies of the half of the deuteron energies are produced [46]. The highest reaction cross sections are achieved at deuteron energies above 10 MeV. The neutron yield is peaked in a forward direction and the neutron beam has a sub-nanosecond pulse duration. For an efficient laser-driven acceleration of deuterons ultra-high-contrast and ultra-high-intense PW-class laser systems are demanded [46, 47]. In the proton induced reactions, a compound nucleus is excited. The interaction of protons with light isotopes results in a flat neutron spectrum. This is different from the interaction of protons with heavy isotopes, where the neutron spectrum peaks at low energies. The realization of a laser driven spallation neutron source needs several tens of MeV proton energies. State-of-the-art research on these neutron production concepts are presented in [46, 48, 49].

In the case of photo-nuclear reactions, compound nucleus excitations take place. The neutron spectrum can be described by a Boltzmann-like distribution function with a mean kinetic energy up to several MeV and an isotropic angular distribution. Depending on the neutron generation process, the neutron source properties differ from each other in the energy distribution, the directionality and the pulse duration. Compared to the proton/deuteron induced neutron generation processes, the pulse duration of the gamma-driven neutrons is much shorter [50, 51] due to the relativistic feature of the electron beam generating γ -rays. Nowadays, the high-yield laser-driven γ and neutron-beam production schemes are based on applications of high-intensity multi-petawatt-class laser systems, where the current state-of-the-art research is discussed in [50, 51].

We present a novel experimental scheme for generating ultra-intense γ and neutron beams at moderate relativistic laser intensities and set record values of γ and neutron fluences.

II. EXPERIMENT

Laser driven electron beams are excellent tools for the generation of ultra-short and bright sources of particles and radiation. Experimental results on enhanced laser driven beam generation in the multi-MeV energy range in interaction of sub-ps laser pulses of relativistic intensities with sub-mm thick low-density polymer foams promise a strong increase of the diagnostic potential of high-energy sub-PW and kJ PW-class laser systems [52–54].

In the experiment, a high energy sub-picosecond laser pulse of relativistic intensity interacts with a pre-ionized polymer foam of near critical electron density (NCD), where super-ponderomotive electrons are produced via the direct laser acceleration (DLA)-process in the presence of strong quasi-static electric and magnetic fields [55, 56]. A radial electrostatic field is created by ponderomotive expulsion of background plasma electrons caused by a relativistic laser pulse. At the same time, the current of accelerated electrons generates an azimuthal magnetic field [56]. A relativistic electron trapped in the channel experienced transverse betatron oscillations and gains the energy efficiently from the laser pulse when the frequency of the betatron oscillations becomes in resonance with the Doppler shifted laser frequency [56].

The DLA works efficiently in NCD plasmas and with a picoseconds laser pulse duration. Different from the laser wake field acceleration (LWFA), the DLA does not generate electrons at very high energies, rather, it produces ample amounts of electrons with Maxwell-Boltzmann-like distributions carrying μC of charge [55, 60, 61]. The interaction of a high number DLA-accelerated electrons with high- Z materials causes an ultra-high fluence of MeV-radiation that can trigger nuclear reactions resulting into neutron production.

The effective temperature of the DLA accelerated electrons exceeds more than one order of magnitude the ponderomotive potential and their energies extend up to 100 MeV, already at moderate relativistic laser intensities [53, 54]. The reason for this behavior is a long acceleration path in a NCD plasma ensured by pre-ionized sub-mm thick foams and a relatively long sub-ps laser pulse duration. This differs from the case of the so-called multilayer targets where a low-density (“near-critical”) layer of a few-micron thickness is added on the illuminated side of a thin, high-density layer. Such kind of a target was used in the last decade for proton acceleration at ultra-relativistic intensities and sub 100-fs pulses [69–71]. In [70], the generation of hot electrons from a double layer target irradiated by a laser pulse with an intensity of $2 \times 10^{20} \text{ W/cm}^2$ was reported. The target consisted of a several micrometer thin NCD plasma slab ($0.5 n_{cr}$) an over-dense foil. The measured effective electron temperature was of 8 MeV, what is only twice higher than the ponderomotive potential.

The present experiment was performed at the high-energy laser facility PHELIX [57]. We investigated the electron acceleration with the focus on the secondary γ

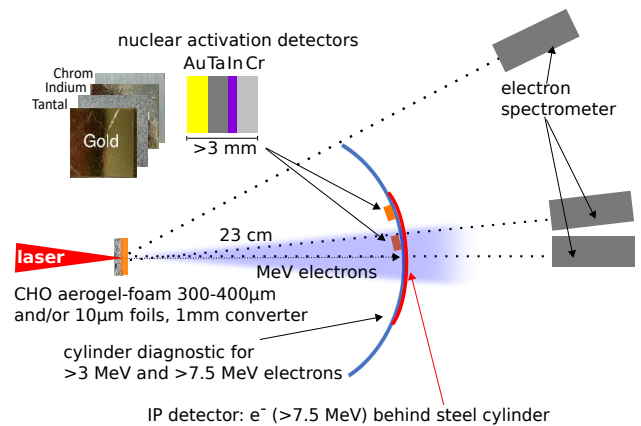


FIG. 1. **Experimental set-up.** Top view of the diagnostic set-ups used for irradiation of aerogel-foams at 10^{19} W/cm^2 (20 J in focal spot) laser intensity and conventional foils at ultra-relativistic intensity of $\sim 10^{21} \text{ W/cm}^2$ (40 J in focal spot). An imaging plate behind 6 mm thick steel cylinder was used to measure an angular distribution of electrons with energies $>7.5 \text{ MeV}$. Nuclear activation plates consisting of different materials were placed at the front of cylinder at 5° and 15° to the laser axis. Three 0.99 T magnet spectrometer measured the energy distribution of accelerated electrons at 0° , 15° and 45° to the laser axis.

and neutron generation using two different peak laser intensities ($\sim 10^{19} \text{ W/cm}^2$ and $\sim 10^{21} \text{ W/cm}^2$). These different intensity regimes were achieved by different focusing systems [54]. Polymer aerogel-foams with a mean density of 2 mg/cm^3 and sub-millimeter thickness [58] were used for the production of a NCD-plasma via the mechanism of super-sonic ionization [53, 59] by sending a well-controlled nanosecond-pulse before the main relativistic pulse. A fully ionized plasma corresponds to $0.64 \times 10^{21} \text{ cm}^{-3}$ electron density or $0.64 n_{cr}$ ($n_{cr} = 10^{21} \text{ cm}^{-3}$). Measurements of the plasma density inside the ringholder after ionization by a super-sonic wave is a big challenge. At the same time, PIC-simulations performed for a step-like density profile with n_{cr} and $0.5 n_{cr}$ [60, 61] as well as for a partially ramped density profile in order to account for plasma expansion toward the main laser pulse [53] showed a very similar overall behavior of the energy and angular distributions of super-ponderomotive electrons. Compared to NCD-plasmas generated by laser irradiation of conventional foils, the DLA path in 300–400 μm thick foams is strongly enhanced, which results in an increased propagation length of the laser main pulse through the NCD-plasma and allows to produce a high charge of electrons with energies far above the ponderomotive potential [53]. A schematic of the experimental setup is presented in Fig. 1. Here, the energy distribution of the DLA-electrons was measured by means of magnet spectrometers. A steel cylinder was used to map the angular distribution of the electron beam. The high-current well-directed super-ponderomotive electrons produced in the NCD plasma pass through a high- Z converter generating bremsstrahlung. γ -rays together with some fraction

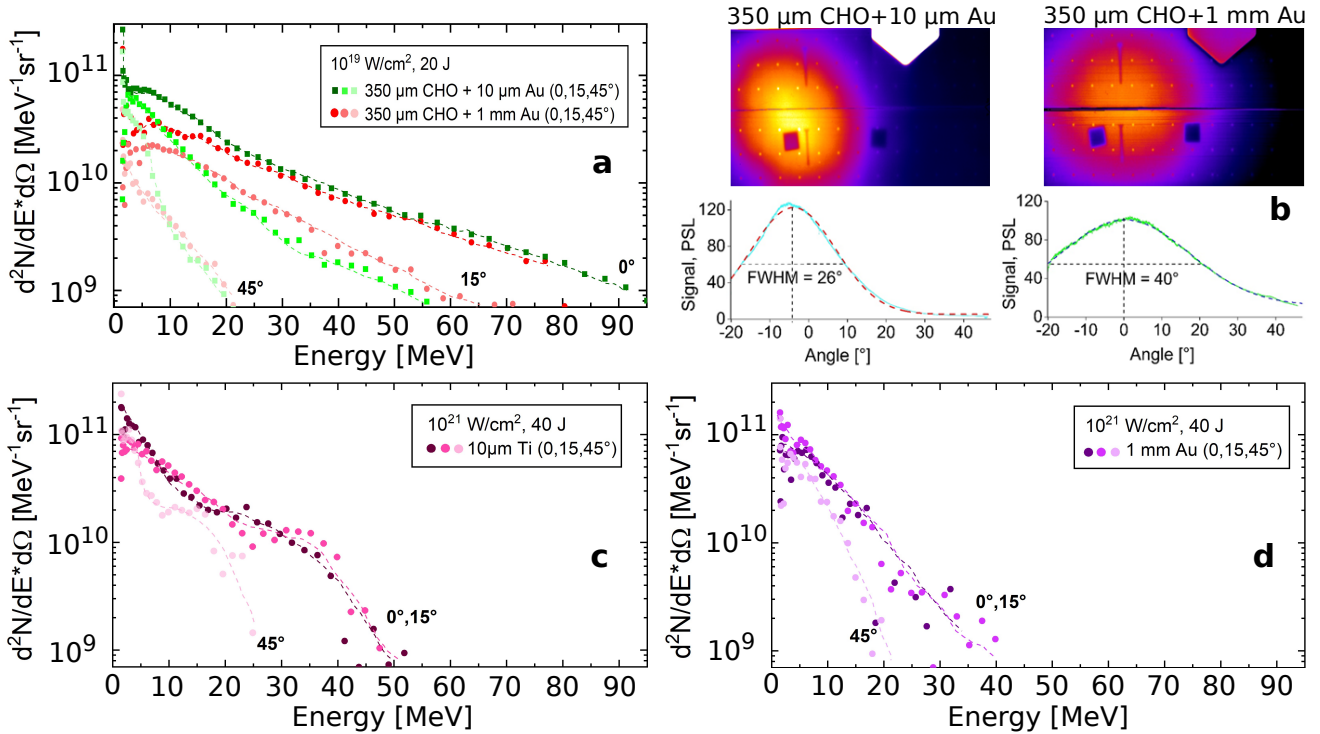


FIG. 2. **Electron spectra.** Electron spectra measured at three different angular directions to the laser axis (0° , 15° , 45°) produced in laser interactions with intensities and laser energies contained in the FWHM of the focal spot. (a) Spectra from laser interaction at 10^{19} W/cm 2 , 20 J in focal spot with aerogel target stacked together with $10\ \mu\text{m}$ gold foil (setup 1a, green) and with 1 mm gold converter (setup 1b, red). (b) Result of the cylinder stack diagnostic for the angular distribution of super-ponderomotive electrons with energies >7.5 MeV measured in a single shot onto an aerogel+thin foil and aerogel+thick converter. (c) Spectra from interactions at 10^{21} W/cm 2 , 40 J in focal spot with $10\ \mu\text{m}$ titanium foil and (d) 10^{21} W/cm 2 , 40 J in focal spot with 1 mm gold converter.

of relativistic electrons that escape the converter, propagated 23 cm in vacuum and trigger nuclear reactions in the activation detectors consisting of Au, Ta, In and Cr.

For further discussion, we introduce the convention for the designations of the four principal laser-target setups used in the experiment, which will be applied in the following: **setup 1a** (10^{19} W/cm 2 onto foam+thin foil), **setup 1b** (10^{19} W/cm 2 onto foam+1mm thick foil), **setup 2a** (10^{21} W/cm 2 onto thin foil), **setup 2b** (10^{21} W/cm 2 onto 1mm thick foil).

III. RESULTS AND DISCUSSION

Electron spectra. In the experiment, spectra of super-ponderomotive electrons were measured by means of magnetic spectrometers at three different angles to the laser axis (see Fig. 1). In the case of setups 1a and 1b, we observe a strong dependence of the electron energies on the angle between the electron beam propagation direction and the laser direction, which is presented in Fig. 2a. The experimental graphs are shown for the electron spectra measured at 0° , 15° and 45° to the laser axis for setup 1a (green) and setup 1b (red). The main fraction of rel-

ativistic electrons is accelerated along the laser axis (0°) up to energies of 100 MeV (Fig. 2a). The difference in the spectra between setups 1a and 1b is caused by propagation of electrons through 1 mm thick Au-converter in the 1b-case. This thickness corresponds to the mean free path of electrons with $E \leq 8$ MeV.

The electron energy distribution was approximated by a Maxwellian-like distribution function with one or two effective temperatures T_{hot} . In the case of setup 1a, the electron spectrum measured at 0° was described by an exponential function with $T_{\text{hot},1} = (12.1 \pm 1.4)$ MeV and $T_{\text{hot},2} = (26.5 \pm 3.4)$ MeV, both exceeding the ponderomotive potential at 10^{19} W/cm 2 more than order of magnitude. With increasing the observation angle, the temperature and the number of accelerated electrons drop down to $T_{\text{hot},1} = (8.1 \pm 1.2)$ MeV ($T_{\text{hot},2} = (15.8 \pm 1.7)$ MeV) at 15° and further to $T_{\text{hot},1} = (1.9 \pm 0.1)$ MeV ($T_{\text{hot},2} = (7.3 \pm 1.2)$ MeV) at 45° .

Fig. 2b presents results of 120° -cylinder diagnostic (see methods) for setups 1a and 1b. The Imaging Plate (IP) signals are caused by electrons with $E > 7.5$ MeV, which are capable to trigger nuclear reactions in activation samples. The measurements show that in the first case, the relativistic DLA electrons with energies above 7.5 MeV propagate within a half angle of 13° to the laser

axis (0.16 sr solid angle), while in the set-up 1b within 20° (0.38 sr) due to electron scattering in 1 mm thick foil.

In direct shots on thin metallic foils at ultra-relativistic laser intensity of 10^{21} W/cm² (setup 2a), the electron energy distribution was approximated with $T_{\text{hot}}=9.9\pm 2.2$ MeV (Fig. 2c) for measurements at 0° and 15° to the laser axis and the maximum of the detected electron energy reached 50 MeV. In shots onto 1 mm thick converter (setup 2b), the effective temperature and the maximum of the detected energy of escaping electrons are 4 MeV and 40 MeV correspondingly (Fig. 2d). A weak angular dependence of the electron spectra indicates a rather divergent electron beam.

MeV γ beam. For the characterization of the bremsstrahlung spectrum generated by super ponderomotive electrons in high- Z samples, we used a nuclear activation-based diagnostic, which is sensitive to >7.5 MeV photon energies, similar to that described in [62]. In the present work, the samples composed of elementary Au, Ta, In and Cr were stacked together and placed at a distance of 23 cm in forward direction at 5° and 15° to the laser axis (Fig. 1).

After each laser shot, the nuclear activated samples were analyzed by a low-background spectroscopy using 60% high purity germanium (HPGe) detector systems to identify the reaction channels leading to the isotopes of interest (see Fig. 7, methods) and to determine reaction yields of the activated isotopes in every sample (Fig. 8c, d). The high-energy bremsstrahlung spectrum was evaluated according to the analysis process described in Methods.

Figure 3 shows the energy dependent bremsstrahlung fluences detected at 5° to the laser axis for the different laser intensities and target systems (setup: 1a,1b, 2a, and 2b). In the case of setup 1b, the photon spectrum follows an exponential dependence on energy with an effective temperature of (12.7 ± 2.1) MeV. A measured number of photons reaches $(4.9\pm 2.1)10^9$ per 1.5×1.5 cm² area of the activation sample stack or $(1.2\pm 0.5)10^{12}$ ph/sr. We would like to point out, that only in interaction of 10^{19} W/cm² laser pulse with a foam layer stacked together with 1mm thick Au-converter (1b), photo-neutron disintegrations up to $^{197}\text{Au}(\gamma,5n)^{192}\text{Au}$ with maximum of the reaction cross section at 50 MeV (Fig. 8a) were observed (red dots at 50 MeV, Fig. 3). In the case of direct irradiation of a high- Z converter with ultra-relativistic laser intensity (setup 2b), a 10 times lower fluence of $(1.2\pm 0.5)10^{11}$ ph/sr with a twice lower effective temperature of (5.3 ± 2.0) MeV was reached compared to 1b (see Fig. 3). Here, only $(\gamma,3n)$ -reactions in Au and Ta with maximum of the reaction cross section at ~ 30 MeV were registered.

The difference in the photon fluences and effective temperatures in 1b- and 2b- cases can be explained by higher electron energy and directionality of the relativistic electron beam generated in the interaction of 10^{19} W/cm²

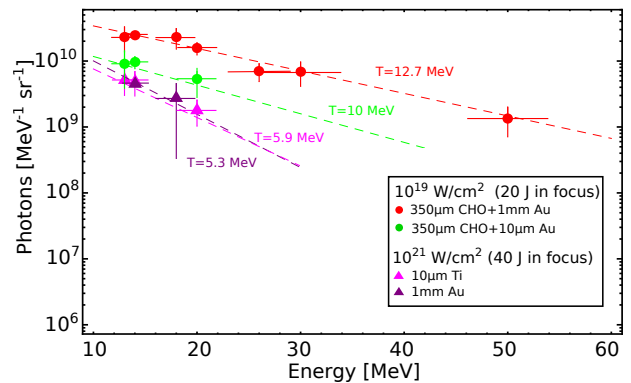


FIG. 3. **MeV-bremsstrahlung.** MeV-bremsstrahlung fluence depending on the energy from different laser-target setups. Dashed lines are thermal exponential fits on the experimental data. The enhancement effect caused by the direct laser acceleration process of electrons in NCD plasmas is observed in the bremsstrahlung generation.

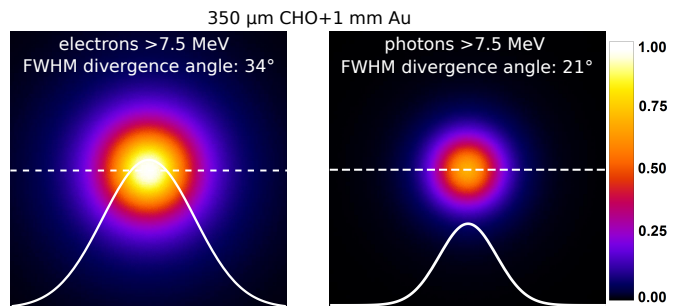


FIG. 4. **Simulated angular distribution.** GEANT4 simulations of the angular distribution of electrons and photons >7.5 MeV after the laser pulse interaction with an aerogel-foam target combined with a 1 mm thick converter. The angular distributions are shown using the same color scale in arbitrary unit. The half divergence angle of the electron beam is 17° , where the photons are distributed within the half divergence angle of 10.5° . The white curves represent the line-out (dashed lines) of the colored distribution.

(20 J) laser pulse with pre-ionized sub-mm thick foam targets compared to shots with an ultra-relativistic intensity of 10^{21} W/cm² (40 J) onto Au-converter (see Fig. 2a and 2d).

The bremsstrahlung spectra measured by means of the nuclear activation method in setups 1b and 2b consist of a primary gamma-beam with $E>10$ MeV (threshold of photo-nuclear reactions), generated by laser-accelerated electrons in the Au-converter, and a secondary γ -beam, produced by >10 MeV electrons that emerge the converter (see Fig. 1, experimental setup) and hit the activation stack. The acceptance angle of the activation sample stack is of 4.3 msr, only. This is a small part of solid angles covered by the relativistic electron and γ beams. In the case of 1b, the divergence angle of electrons was defined experimentally (Fig. 2b), the divergence angle of the >10 MeV γ beam generated in the converter

was unknown.

In order to solve this problem, the GEANT4 Monte Carlo code [63] was used to simulate the relativistic electron transport through a 1 mm thick converter (setup 1b) and the generation of the primary gamma-beam. The experimental geometry together with the measured energy and angular distributions of the DLA-electrons in the case of setup 1a were used as input parameters. The benchmarking was done by comparing measured and simulated isotope yields (see Fig. 8c). Simulations resulted in a half divergence angle of 17° (0.27 sr) for electrons above 10 MeV and 10.5° (0.11 sr) for γ of the same energy (see Fig. 4). This means that in the case of setup 1b, 1.6% of electrons and 4% of primary gammas generated in 1mm Au converter interact with the activation samples and trigger nuclear reactions. In addition, in the sample placed at 15° , a more than one order of magnitude lower activity was measured, which also indicates a highly directed MeV-bremsstrahlung beam. The differences between the measured (0.38 sr, Fig. 2b) and the simulated (0.27 sr) electron divergence cones can be explained by a strong increase of the IP-response produced by electrons with energies below 1 MeV [64] compared to those >1 MeV. The simulations also show that 55% of initial electron beam is converted into the primary γ beam in the converter and 30% into the secondary γ beam by propagation through the activation sample stack.

Based on these results, the estimated total number of photons >10 MeV reaches 1.7×10^{11} . Taking into account the effective temperature of (12.7 \pm 2.1) MeV and laser energy of 20 J, we end up with an ultra-high conversion efficiency of the laser energy into >10 MeV gammas of (1.4 \pm 0.3)%. Compared to the present work, a new concept of a non-linear Compton backscattering scheme driven by a PW short laser pulse at $>5 \times 10^{21}$ W/cm² in a NCD plasma coupled with a plasma mirror was recently discussed in [65]. The described simulation studies show a broad-band spectrum that contains $>10^{11}$ photons with energies above 10 MeV with less than 1% laser-to- γ energy conversion efficiency.

Accelerated protons. In laser interactions with thin foil targets at 10^{21} W/cm² laser intensity (setup 2a) and with combined foam and thin foil target systems at 10^{19} W/cm² (setup 1a), we observed proton induced nuclear reactions in the GDR region. These reactions lead to compound nucleus excitations in Au and Cr activation samples and generation of Hg and Mn isotopes. The reaction cross sections and corresponding proton energy ranges of the GDRs are shown in Fig. 8a. In the case of proton-induced reactions, there are no competing photo-nuclear channels that lead to the same isotope if starting from the same natural stable mother isotopes.

For setup 2a, where the activation stack was oriented to laser with Au-sample (Cr is at rear), we observed following proton-driven nuclear reactions: $^{197}\text{Au}(p,n)^{197m}\text{Hg}$ with a maximum of the cross section at 12 MeV proton energy, $^{197}\text{Au}(p,3n)^{195m}\text{Hg}$ at 14 MeV and $^{54}\text{Cr}(p,3n)^{52}\text{Mn}$ at 37 MeV. In the case of setup

1a, with an opposite sequence of samples (Cr is at front), $^{197}\text{Au}(p,n)^{197m}\text{Hg}$, $^{52}\text{Cr}(p,n)^{52}\text{Mn}$ at 14 MeV, and $^{54}\text{Cr}(p,3n)^{52}\text{Mn}$ nuclear reactions were identified.

The proton number within the width of each GDR was deduced from the reaction yield of the corresponding isotope by deconvolution with the reaction cross sections (see Fig. 8a). The proton number measured in the GDR region per sample centered at 14 MeV with the resonance width of 8 MeV and at 37 MeV with the resonance width of 20 MeV are $(1.38 \pm 0.62) \times 10^9$ and $(1.48 \pm 0.80) \times 10^9$ for the setup 1a. In the case of setup 2a, the proton number reached $(1.62 \pm 0.41) \times 10^{10}$ at 14 MeV and $(3.74 \pm 1.03) \times 10^8$ at 37 MeV proton energy. Compared to setup 2a at 10^{21} W/cm² and laser pulse energy of 40 J, the proton number in setup 1a at 10^{19} W/cm² with 20 J laser energy reaches a 4 times higher value in the upper cut-off region of proton energy. This behavior allows for enhanced nuclear reaction yields over a wide range of proton energies.

Figure 5a shows normalized proton number in dependence on the energy obtained for setups 1a (green) and 2a (magenta). In the case of interaction of 10^{21} W/cm² laser pulse with a thin foil (setup 2a), experimental data were fitted by an exponential function with an effective temperature of 5-6 MeV. This protons spectral properties are characteristic for the TNSA mechanism [67, 68]. The important feature of the proton spectrum evaluated for setup 1a is a very flat slope (Fig. 5a, green dashed line), which results into a high proton number at energies above 20 MeV. The dark blue curve in Fig. 5a presents the result of the 3D PIC simulation performed by means of the virtual laser plasma laboratory (VLPL) code [66] for the experimental conditions discussed in Sec. II. The slope of the simulated proton spectrum is in a good agreement with the experiment.

Another important feature of the proton beam in the case of setup 1a is its low divergence. We measured a 500 times higher ^{52}Mn isotope yields produced in the activation stack (Cr-front) placed at 5° to laser axis compared to those measured at 15° . In these shots, the target normal was counterclockwise rotated by 10° to laser direction (Fig. 5b). The half protons divergence angle of 6° - 7° was estimated assuming a Gaussian angular distribution of the proton beam centered at the target normal and taking into account proton driven reaction yields measured at 5° and 15° .

This is in a good agreement with 3D PIC results. According to the simulations (setup 1a), the 20 J laser pulse is absorbed in the foam before it reaches the foil [54]. A large space charge of super-ponderomotive electrons accelerated in the NCD-plasma reaches the rear side of the foil, which stays cold. The simulations show that energetic electrons spread out along the foil rear side generating a very planar electrostatic field. This field accelerates a highly collimated ion beam. Result of simulations is presented in the diagram of the longitudinal and transversal proton momenta (Fig. 5c), which is characteristic for a highly collimated proton

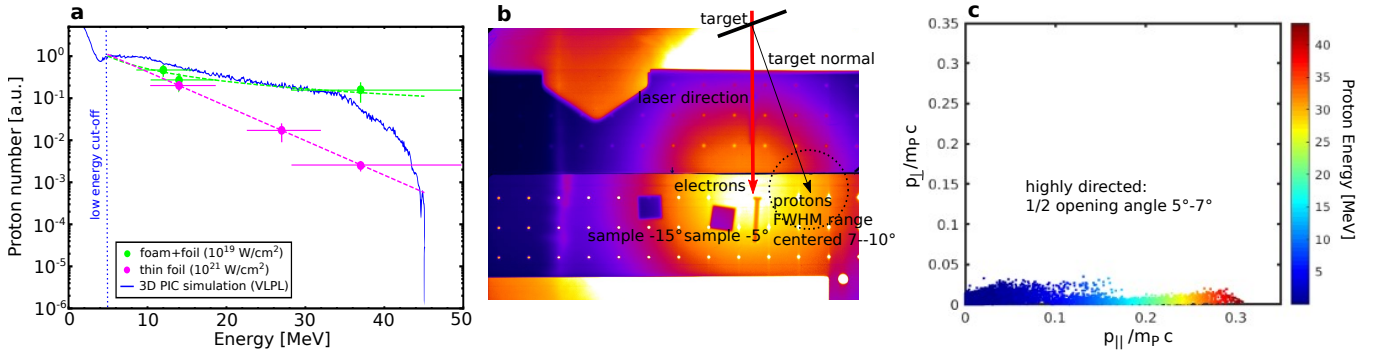


FIG. 5. **Protons.** (a) Proton number in arbitrary units as a function of proton energy. Green dots are proton number evaluated in case of laser interaction with aerogel-foams combined with thin metal foils at 10^{19} W/cm 2 intensity (setup 1a), while the magenta dots show protons from laser interactions with thin metal foils at 10^{21} W/cm 2 laser intensity (setup 2a). The dashed curves are model functions, which fit the slope of the proton spectra. PIC-simulated proton spectrum is shown as blue solid line. (b) Electron angular distribution (>7.5 MeV) and position of activation samples in case of setup 2a. Target normal was $+10^\circ$ to laser direction. The half protons divergence angle of 6° - 7° was estimated assuming a Gaussian angular distribution of the proton beam centered at the target normal and taking into account proton driven reaction yields measured at 5° and 15° (black dotted circle). (c) Momentum diagram of protons from 3D PIC simulation (VLPL code).

beam with a 5° - 7° half of divergence angle.

Neutrons. Enhanced neutron fluences were observed in laser pulse interactions with foam target systems at moderate relativistic laser intensities. Here, in the setup 1a, neutron generation was dominated by protons, while in the setup case 1b the neutrons are dominantly generated by photo-nuclear reactions.

In both cases, the generation of neutrons was investigated via a well-established indium activation method (e.g. [73]), which can be applied for fast and epithermal/slow neutrons. In the experiment, elementary indium with a purity of 99.999 % in the natural isotope abundance of ^{115}In (95.7 %) and ^{113}In (4.3 %) was used. We focused on the decay channels of activated indium isotopes that were reached via neutron induced reactions. In this procedure, an input of γ -driven nuclear reactions leading to the same indium isotope type was taken into account (see Fig. 8d).

In the study of reactions triggered by epithermal neutrons, the strong nuclear resonance with a reaction cross section of 10^4 barn at 1 eV for the neutron capture reaction $^{115}\text{In}(n,\gamma)^{116m}\text{In}$ was considered. Fast neutrons were investigated by the pure neutron activation channel $^{115}\text{In}(n,n')^{115m}\text{In}$ with 0.343 barn at 2.5 MeV and the activation channels $^{113}\text{In}(n,n')^{113m}\text{In}$ with 0.2 barn at 2.5 MeV as well as the $^{113}\text{In}(n,2n)^{112m}\text{In}$ reaction with 1.5 barn at 14 MeV initial neutron energy. The reaction channels $^{115}\text{In}(n,2n)^{114m}\text{In}$ and $^{113}\text{In}(n,\gamma)^{114m}\text{In}$ are not useful because the daughter isotope becomes the same for fast and slow neutrons.

The neutrons were produced within the activation sample placed at a distance of 23 cm to the laser interaction point, which covers a solid angle of 4.3 msr. The contribution of background neutrons to the produced and detected neutrons within the sample is negligible, which

also results from GEANT4 simulations (see methods).

In the case of setup 1b only, we observed a significant yield of ^{112m}In and ^{114m}In isomers produced by fast neutrons generated in γ -driven nuclear reactions triggered by a high number of >10 MeV photons (Fig. 3, setup 1b). Such reactions lead to the production of neutrons, which are evaporated with high kinetic energy from an excited compound nucleus.

Figure 6 shows the neutron number per activation sample evaluated using the indium isotope yields after subtraction of the γ -driven channels. The energy distribution of neutrons evaporated from excited states of compound nucleus can be described by a Maxwellian like function [74]. The neutron number per energy width of the corresponding GDR was determined by weighting the reaction yields with the cross sections [75] for each reaction. As described in the methods, the mean neutron energy E_{mean} was evaluated by an isotope relation equation using the experimentally measured reaction yields of indium isotopes produced by epithermal as well as fast neutrons starting from the same mother isotope [73]. Then, the Maxwellian-like distribution function is build using the known E_{mean} and measured neutron number. The dashed curves in Fig. 6 present such neutron distribution functions for each scenario.

In the case of setup 1b (Fig. 6, red dots), the enhanced neutron production centered at fast neutrons is explained by a higher effective temperature and fluence of the MeV-bremsstrahlung (see Fig. 3). In this case, we observe neutron activations in indium around 14 MeV neutron energy.

In the setups 1a and 2a, using thin foils, neutrons were produced by proton induced nuclear reactions. Only in the case of setup 1a, we observed a high number of ^{116m}In generated in interactions with epithermal/slow neutrons (Fig. 8d) and ^{112m}In activations at 14 MeV neutron en-

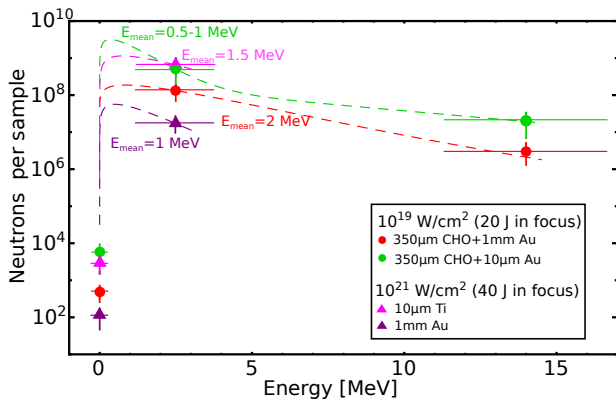


FIG. 6. **Neutrons.** Number of neutrons in different GDR regions measured in the activation sample with 4.3 msr acceptance angle for different laser-target setups. The mean neutron energies E_{mean} are evaluated from the activation method (see methods) and used to build a Maxwellian-like energy distribution of neutrons (dashed lines).

ergy. This behavior is a consequence of the flat slope of the proton spectrum, which leads to a high proton number at energies >20 MeV responsible for fast neutron production. The observed reaction yields fit well with GEANT4 simulations (see methods, Fig. 8d).

In addition to the indium isomer activation, we observed neutron capture reactions in the Au sample ($^{197}\text{Au}(n,\gamma)^{198m}\text{Au}$) induced by epithermal neutrons at 5 eV, where a strong resonance with a cross section of 2.8×10^4 barn was excited. The highest yield of ^{198m}Au was observed for the laser-target setup 1a, where the mean kinetic energy of neutrons generated in proton driven nuclear reactions was of 0.5–1 MeV. The stable Au isotope represents a waiting point within the nuclear astrophysical r-process heavy element nucleosynthesis. Within the experimental accuracy, the ^{198m}Au yield reached in the present work is in a good agreement with the theoretical study by Hill et al. [30].

Summarizing results, we suggest an universal approach for the strongly enhanced laser-based generation of an ultra-high neutron fluence triggered by gammas and/or protons using foam-foil target systems. Keeping the laser parameters constant and varying the target systems one can create two neutron production schemes:

1. In the case of aerogel-foam targets combined with $10\mu\text{m}$ Au foils, the neutron generation is dominated by proton induced nuclear reactions. The neutron number evaluated from the proton-driven nuclear reactions in the sample with 4.3 msr acceptance angle reaches $(6.7 \pm 0.8) \times 10^9$ per shot, while the mean neutron kinetic energy was of 0.5 – 1 MeV. Triggered by all accelerated protons propagating in the solid angle of 0.04 sr the neutron number reaches $(6.2 \pm 0.5) \times 10^{10}$ per laser shot.

2. Using aerogel-foams stacked with high-Z converters (setup 1b), the neutron generation via photo-nuclear reactions in the sample is caused by high fluence electrons

and γ 's with $E > 10$ MeV. The evaluated neutron number is of $(3.6 \pm 0.6) \times 10^8$ per shot and a mean neutron kinetic energy of 2 MeV. The number of neutrons triggered by all initial electrons and photons above 10 MeV propagating in 0.27 sr and 0.11 sr solid angles (Fig. 4) reaches $(1.4 \pm 0.2) \times 10^{10}$ per laser shot.

The high nuclear reaction yield in the case of aerogel targets and the corresponding total fluence and temperature of γ photons as well as mean kinetic energy of neutrons is realized by the strong enhancement of the number and the energy of super-ponderomotive electrons compared to shots onto foils at ultra-relativistic intensity.

In Tab. I, the results of the present work are shown in comparison with previous experiments on laser-driven neutron sources, where record values were reported in two independent neutron production schemes described by Roth et al. and Jung et al. [46, 47], Kleinschmidt et al. [49], and by Pomerantz et al. [50]. In the present work, using the combination of low density foams with thin or thick metallic foils, two neutron generation schemes were realized: one via pure γ induced nuclear reactions and another one, via proton dominated nuclear reactions, which results in a high neutron fluence.

In setup 1b, a high current beam of super-ponderomotive electrons boosts the production of MeV-bremsstrahlung radiation by propagation through a high-Z converter. In this scheme, a record conversion efficiency of laser energy into energy of >10 MeV γ -rays of $(1.4 \pm 0.3) \%$ was achieved. The measured 1.4×10^{10} neutrons with 2 MeV averaged energy correspond to 0.02 % laser-to-neutron conversion efficiency. In [50], super-ponderomotive electron beams were used to trigger neutron production in Cu-converter. The relativistic electrons were generated at 5×10^{20} W/cm² laser intensity and 90 J laser energy on target in interaction with underdense CH-plasma. The number of registered neutrons and the corresponding conversion efficiency were more than 10 times lower than in our case (see Tab. I).

The more efficient neutron production scheme can be realized via proton and deuteron induced nuclear reactions. In our experiment, using foam+thin foil (setup 1a), we observed enhance generation of protons in the GDR region >20 MeV and measured 6.2×10^{10} neutrons with 0.5–1 MeV averaged energy. The laser-to-neutron conversion efficiency of 0.05 % exceeds results reported in [46, 47] and is close to those obtained at the PHELIX-laser by Kleinschmidt et al. [49] using deuteron induced nuclear reactions. Note that in these experiments, results were obtained at higher laser energies and at 10–50 times higher laser intensities than in our case.

An additional advantage of our approach realized via proton beams, is the generation of a high number of neutrons with moderate kinetic energies, which can be applied in experiments on laboratory astrophysics. Confirmation of this is the observation of the high yield of ^{198m}Au produced in the neutron capture process.

In summary, the interaction of a sub-ps laser pulse of moderate relativistic intensity with sub-mm long poly-

	p -driven (this work)	γ -driven (this work)	ion-driven [46, 47]	ion-driven [49]	γ -driven [50]
laser intensity I_{laser}	$\sim 10^{19} \frac{W}{cm^2}$	$\sim 10^{19} \frac{W}{cm^2}$	$5 \times 10^{20} \frac{W}{cm^2}$	$2 \times 10^{20} \frac{W}{cm^2}$	$2 \times 10^{20} \frac{W}{cm^2}$
focused energy E_{laser}	20 J	20 J	52 J	60 J	90 J
target system	CHO foam	CHO foam	CD ₂ foil	CD ₂ foil	CH foil
neutron production	(p, xn)	(γ, xn)	(d, n)	(d, n)	(γ, xn)
primaries (>10 MeV)	$\sim 3 \times 10^{11}$, proton	3×10^{11} , e^-	$> 10^{11}$, d	N/A, d	N/A, e^-
laser-primary conversion eff.	–	10 %	0.5 %	N/A	N/A
laser- γ conversion eff.	–	1.4 % (>10 MeV)	–	–	N/A
total neutron number	6.2×10^{10}	1.4×10^{10}	7.2×10^9	6.5×10^{10}	1.2×10^9
neutron direction	isotropic	isotropic	16 % directed	10 % directed	isotropic
mean neutron energy	500 keV – 1 MeV	2 MeV	>10 MeV directed 2–4 MeV isotropic	>10 MeV directed 2–4 MeV isotropic	~ 1 MeV
laser-neutron conversion eff.	0.05 %	0.02 %	0.01 %	0.07 %	0.0002 %
neutrons per laser energy	3.1×10^9 n/J	7×10^8 n/J	1.3×10^8 n/J	1.07×10^9 n/J	1.3×10^7 n/J

TABLE I. **Conversion efficiencies.** Results from presented work in case of γ -neutron production and proton-driven neutron generation are shown in comparison with previous experiments, where records of neutron generation via laser accelerated deuterons interacting with beryllium catcher [46, 47, 49] as well as via the electron acceleration to bremsstrahlung to neutron scheme [50] were reported.

mer foams combined with thin and thick high- Z foils results into the highest number of generated neutrons per Joule laser energy compared to the schemes presented in Tab. I. This concept promises a strong boost of neutron production on kJ PW-class laser systems.

IV. CONCLUSIONS

In conclusion, we have presented a novel way for producing well-directed high intense multi-MeV γ beams as well as ultra-high fluence neutron sources at moderate relativistic laser intensities of 10^{19} W/cm² and 20 J energy within the focal spot. Our approach is based on the DLA-process in long-scale NCD plasmas, where the super-ponderomotive electrons with energies up to 100 MeV are produced. The charge carried by electrons with >10 MeV propagating in the 0.16 sr solid angle reaches 50–100 nC what corresponds to 10% of the conversion efficiency. This high-current well-directed electron beam is the basis for the generation of proton- and γ -sources applicable for the discussed nuclear research.

Ultra-high intense, highly directed MeV γ beams with fluences of $> 10^{12}$ ph/sr above 10 MeV photon energy and effective temperatures of 13 MeV were detected. The conversion efficiency from laser energy into >10 MeV-photons reached (1.4 ± 0.3) %. This provides a basis for the preparation of a narrow band γ beam, suitable for nuclear photonics applications [7, 76].

The presented experimental technique allows to choose the generated neutron behavior by varying the target system. Depending on the application needs, the laser driven neutron source of ultra-high fast neutrons can be provided via photo-nuclear reactions with a laser energy

conversion efficiency of 0.02 %. Higher laser to neutron conversion efficiency of 0.05% was achieved via proton induced neutron generation already at moderate relativistic laser intensities and ps pulse duration, where the averaged neutron energies are in a suitable range for nuclear physics applications without moderation processes. New experimental top yields, realized in the present work at 10^{19} W/cm² laser intensities and 20 J laser energy, reached $> 10^{10}$ neutrons per laser shot in the photon-driven as well as $> 6 \times 10^{10}$ per shot in the proton-driven scheme. The shape of the neutron spectra evaluated in this work for (p, n)-reactions is very similar to those simulated in [29] and discussed for investigation of multiple neutron capture processes in Zr.

GEANT4 Monte Carlo simulations were performed to optimize the neutron production for PHELIX parameters (10^{19} W/cm², $E_{FWHM} = 20$ J, setup 1b). After placing the Au converter direct to the foam rear-side and increasing the converter thickness up to 5–7 mm, a record neutron fluence of 2×10^{11} cm⁻² and 10^{22} cm⁻² s⁻¹ flux estimated for ~ 20 ps neutron pulse duration was achieved. From *Particle-In-Cell* (PIC) simulation studies we expect a more than one order of magnitude higher relativistic electron number with energies above 7.5 MeV by increasing the laser energy from 20 J to 200 J. This results in a corresponding enhancement of the neutron fluence and flux.

Current developments in the laser technology toward higher laser pulse energies and higher repetition rates (one shot per minute) will allow for investigation of multi neutron capture processes in laboratory conditions. Parts of the field for astrophysical nucleosynthesis [77, 78], such as the investigation of the r-process important for the heavy element synthesis in solar or explosive scenarios become accessible. Especially, the investiga-

tion of multi/single neutron capture rates on heavy radioactive or unstable elements is a current challenge and not experimentally accessible in conventionally nuclear physics facilities.

One of the upcoming facilities using radioactive heavy ions is the *Facility for Antiproton and Ion Research* (FAIR) in Darmstadt, Germany [79, 80]. The two most limitations for the feasibility of such nuclear astrophysical studies are: 1. the separation of the heavy ion facilities from reactor or accelerator based neutron sources, and 2. too low neutron fluxes reached by conventional neutron sources. A suitable way that allows such important r-process studies is the combination of laser-driven ultra-high flux neutron sources with future heavy ion facilities like FAIR. Our new insights on neutron generation in relativistic laser interactions with long-scale NCD plasmas as well as simulation studies for target setup improvement show a suitable and realistic way to reach conditions for nuclear astrophysical laboratory science using existing high-energy sub-PW laser systems as well as kJ PW-class laser facilities.

V. METHODS

A. Laser and target system

The experiment was performed at the **P**etawatt **H**igh-**E**nergy **L**aser for heavy **I**on **e**Xperiments (PHELIX) laser system at GSI in Darmstadt, Germany. The Nd:Glas laser amplifier system delivered a s-polarized beam with a central wavelength of 1053 nm and a highest main pulse to nanosecond pre-pulse contrast of $>10^{11}$. The pulse length was (0.75 ± 0.25) ps. The laser pulse was focused by an off-axis copper parabolic mirror on the target under $\approx 7^\circ$ to target normal. To conduct a moderate relativistic intense laser pulse of $(1 - 2.5) \times 10^{19}$ W/cm² a (90 ± 10) J pulse was focused by a focal length of 150 cm on the target, where the FWHM of the elliptical focal spot size was $(12 \pm 2) \mu\text{m} \times (18 \pm 2) \mu\text{m}$. 22 % of the laser pulse energy is contained in the FWHM of the focal spot which results in an energy of (20 ± 2) J on the target. The high intensity laser pulse of 10^{21} W/cm² was produced via a 180 J pulse focused by a parabolic mirror with a focal length of 40 cm. The FWHM of the elliptical focal size was $(2.7 \pm 0.2) \mu\text{m} \times (3.2 \pm 0.2) \mu\text{m}$, where the laser pulse energy within the FWHM was (38 ± 2) J. The long focal length was used in laser shots on aerogel-foam target systems and the short focal length was used in shots on foil targets. To realize a NCD plasma a well-defined long pre-pulse with 1.5 ns pulse duration irradiated the foam target system by a delay of 2 – 3 ns before the main pulse, where the intensity of the pre-pulse was about 5×10^{13} W/cm² and the pulse energy was 1 – 3 J [53]. For the generation of a sub-mm NCD plasma a plastic aerogel target made from triacetate cellulose, $C_{12}H_{16}O_8$, with a volume density of 2 mg/cm³ and a thickness between 300 μm and 400 μm was used [58]. A fully ionized plasma

corresponds to 0.64×10^{21} cm⁻³ electron density or 0.64 n_{cr} ($n_{cr} = 10^{21}$ cm⁻³). As foil targets, 10 μm thick pure metallic foils (Au, Ti) and 1 mm thick pure Au targets were used.

B. Electron diagnostics

The electron spectrometers were realized using a homogeneous magnetic field of 0.99 T created by two parallel positioned flat neodymium permanent magnets. Calibrated imaging plates (IP) from BASF [81, 82] were used as detectors. The spectral resolution was optimized by numerical simulations including the measured two dimensional magnetic field distribution by consideration of an entrance slit with a size of 300 μm (width) \times 1 mm (height). The experimental error in the detection of the electrons was not higher than 2%, which allows for a precise spectral measurement in the electron energy range between 1.75 MeV to 100 MeV. To increase the signal-to-noise ratio and to reduce the MeV-bremsstrahlung background, each spectrometer was shielded in front of the entrance slit by a CuW collimator with 40 mm in length with a 3 mm entrance hole. The spectrometers were positioned in laser forward direction at a distance of 405 mm at 0° , 15° and 45° in the horizontal plane perpendicular to the laser polarization direction. Furthermore, a stack of three steel cylinders with a thickness each of 3 mm and a radius of 200 mm were placed in a distance of 230 mm from the laser interaction target. Between the steel cylinder, IPs were fixed to measure the angular distribution of the electron beam in horizontal as well as vertical directions for two different energy ranges above 3 MeV and above 7.5 MeV.

C. Nuclear diagnostics for MeV bremsstrahlung and neutrons

A stack of pure ($>99\%$) elemental Au, Ta, Cr and In plates was used as an activation detector system, where their natural isotope abundance providing different nuclear reaction thresholds (see Fig. 8a). After each laser shot, the nuclear activated samples were analyzed by a low back ground γ -spectroscopy using 60 % high purity germanium (HPGe) detector systems to identify the reaction channels of the isotopes of interest (Fig. 7), where the reaction yield of the activated isotopes in the sample was measured (Fig. 8c,d). In the activation samples, multi-neutron disintegration reactions were observed, triggered by MeV-photons and particles (Fig. 8a,b). The size of each plate was 15 mm \times 15 mm \times 1 mm, while the thickness of the indium foil was of 0.25 mm. The activation detector stacks were placed in a distance of 230 mm at two different angular positions with respect to the laser axis (5° and 15°). The main uncertainty in determination of the reaction yield is caused by the geometrical detector efficiency error, where the geometry

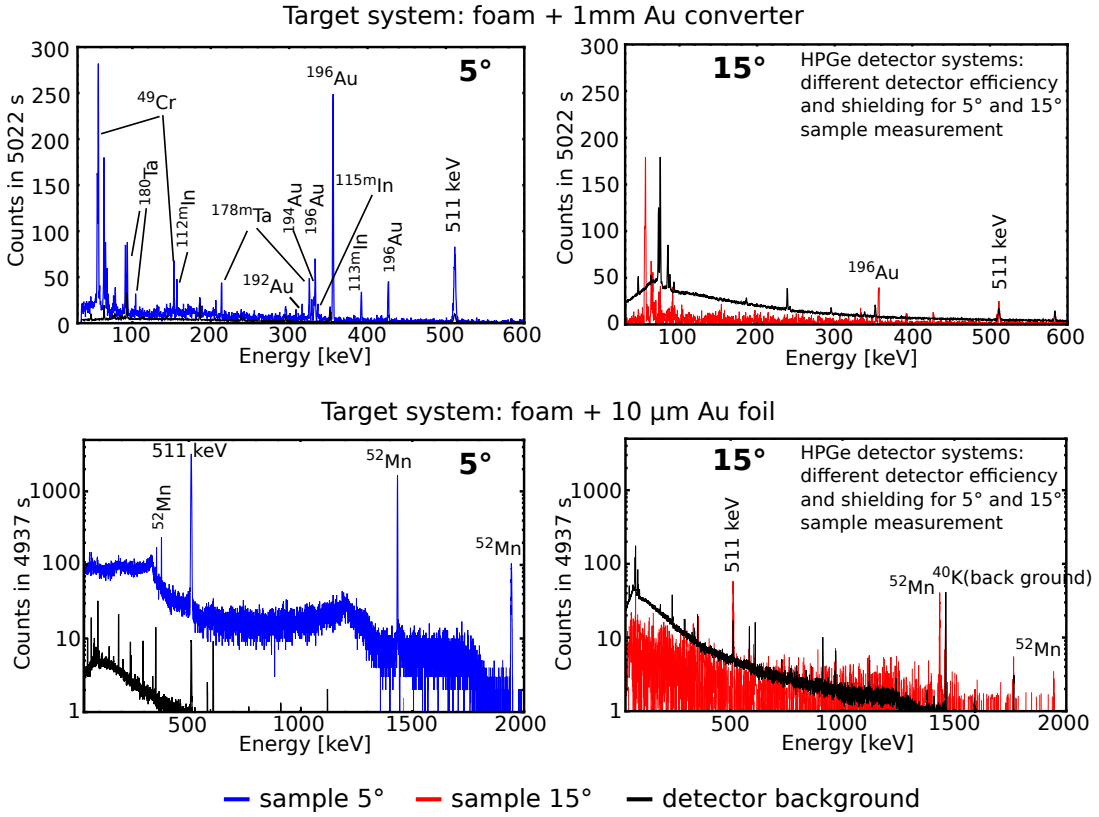


FIG. 7. **Gamma spectrum.** Results of the gamma spectroscopy of the activated samples at 5° (blue spectra) and 15° (red spectra) for the laser-target setup scenarios. The black line in each panel represents the detector background spectrum. The unequal count rate of the background between the panels on left and right is caused by the differently HPGe detector stations with its own back ground shielding. Results are shown after subtraction of the detector background. An important indicator for signal differences between 5° and 15° is the pulse height of the annihilation line at 511 keV, because the most activated isotopes are β^+ -emitter.

and self absorption processes of γ decay lines within the activation samples are considered, and additionally the error of the counting statistics of the HPGe detector. The nuclear reaction yield of each i -th reaction Y_i is the convolution of the initial photon or particle spectrum $N_{\gamma,p}(E')$ with the energy dependent reaction cross section $\sigma_i(E')$ (see Fig. 8a,b): $Y_i = N_T \int_{E_{\text{th}}}^{\infty} N_{\gamma,p}(E') \sigma_i(E') dE'$, where N_T is the surface atomic number density of each sample. The photon or particle spectrum was deconvolve by weighting the reaction yield with the reaction cross section within each energy bin dE' of the reaction i with the reaction threshold E_{th} . The error in the determination of the initial photon or particle spectrum is the combination of the error of the reaction yield and the width of the corresponding nuclear resonance of the nuclear reaction (Fig. 8a,b). All uncertainties are shown as the error bars of the experimental results presented in the corresponding diagrams in this work. The nuclear reaction cross sections were taken from the EXFOR data base [75] and evaluated by the Talys nuclear reaction code [83].

In the following, the indium activation method is described for the neutron fluence measurement. Reaction channels induced by MeV-photons leading to the

same In isotopes with respect to the neutron induced reactions were also considered. The contribution of these reactions is determined by weighting the experimental MeV-bremsstrahlung spectrum (see Fig. 3) with the cross sections (Fig. 8a,b) of the corresponding reaction channels: $^{113}\text{In}(\gamma,\gamma')^{113m}\text{In}$, $^{113}\text{In}(\gamma,n)^{112m}\text{In}$, $^{115}\text{In}(\gamma,\gamma')^{115m}\text{In}$, $^{115}\text{In}(\gamma,n)^{114m}\text{In}$, $^{115}\text{In}(\gamma,2n)^{113m}\text{In}$, $^{115}\text{In}(\gamma,3n)^{112m}\text{In}$. The total γ induced reaction yields of the activated indium isotopes are shown in the right panel of Fig. 8d. For the setups with foam target systems (1a, 1b) the contribution of the γ induced indium isotopes ^{113m}In , ^{112m}In and ^{114m}In are significantly higher compared to the neutron induced same isotopes. However, the γ induced contribution into production of ^{115m}In is more than one order of magnitude lower compared to the neutron induced contribution. The neutron induced reaction yields, shown in the left panel of Fig. 8d, are determined by subtraction of the corresponding yields of γ induced In isotopes from the measured total reaction yields. It has to be noted that the high value of the ^{114m}In yield is reached via the epithermal neutron capture reactions and the fast neutron scattering processes.

Following neutron energy ranges are considered: 1 eV,

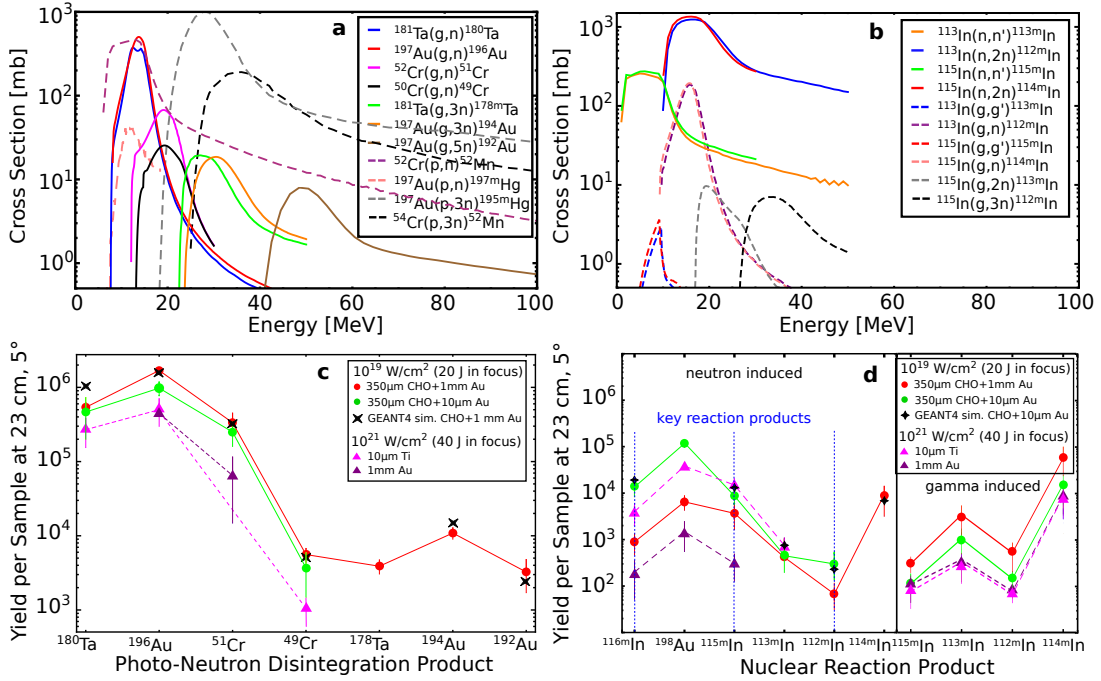


FIG. 8. **Cross section.** (a) and (b) present the nuclear reaction cross sections for the observed gamma, proton and neutron induced reactions. (c) and (d) show the reaction yields. In panel (d) on the left, the pure neutron induced reaction yields are shown for the laser-target setups (these numbers are obtained from the total measured yields after subtraction of yield of the corresponding gamma induced reactions leading to the same isotope). The key reaction products are used for neutron number reconstruction.

2.5 MeV and 14 MeV. This corresponds to three key reaction channels taken into account for the reconstruction of the neutron number: $^{115}\text{In}(n,\gamma)^{116m}\text{In}$, $^{115}\text{In}(n,n')^{115m}\text{In}$ and $^{113}\text{In}(n,2n)^{112m}\text{In}$. The indium isomers ^{113m}In from reactions $^{113}\text{In}(n,n')^{113m}\text{In}$, $^{115}\text{In}(\gamma,2n)^{113m}\text{In}$ and $^{113}\text{In}(\gamma,\gamma')^{113m}\text{In}$, are not used: first, because of the high natural abundance of the stable mother isotope ^{115}In and second, because of the high fluence of γ 's in the corresponding energy range, where the ^{113m}In is produced via γ induced reactions. Also not used for the reconstruction of neutron numbers is the ^{114m}In isomer that is produced via the reaction $^{115}\text{In}(n,2n)^{114m}\text{In}$, because of the activation of ^{114m}In is: first, dominated by γ induced reactions $^{115}\text{In}(\gamma,n)^{114m}\text{In}$ (high γ fluence at 14 MeV, high abundance of ^{115}In) and second, by the neutron capture reaction $^{113}\text{In}(n,\gamma)^{114m}\text{In}$ with a high reaction cross section of 10^4 barn in the epithermal neutrons.

For setup 1a, the simulated reaction yield is exemplary shown in Fig. 8d (black stars). The GEANT4 simulation is in a well agreement to the experimental yields of indium isomers (green dots in Fig. 8d). The simulation considers reactions generated within the sample stack placed at 5° and 23 cm distance from laser interaction point. The ^{116m}In isomers can be also generated by neutron scattering processes on environmental materials. Additional GEANT4 simulations of the background neutron number caused by the target chamber environment resulted into less than 30% contribution to the measured indium isomer yields, what is inside the experimental ac-

curacy.

In the present work, the mean neutron kinetic energy is determined by an advanced isotope relation equation, where the basic idea is taken from [73]. Starting from the ^{115}In mother isotope, the daughter isotopes ^{116m}In activated by thermal/epithermal neutrons and the ^{115m}In activated by fast neutrons are generated. The resonance, excited in the reaction channel $^{115}\text{In}(n,n')^{115m}\text{In}$ is centered in the fast neutron region and overlapping the cross section region of the reaction channel $^{115}\text{In}(n,\gamma)^{116m}\text{In}$ (Fig. 2 in [73]). Therefore, the cross section ratio of the ^{116m}In production to the cross section range of ^{115m}In production is related to the isotope yield ratio of ^{116m}In to ^{115m}In : $\frac{\sigma_{^{116m}\text{In}}}{\sigma_{^{115m}\text{In}}} = \frac{Y_{^{116m}\text{In}}}{Y_{^{115m}\text{In}}}$. The reaction yield of ^{116m}In and ^{115m}In are known from the experiment. Then, the relation equation allows to determine the cross section ratio and therefore the neutron energy where the ^{116m}In isotopes are produced covered by the resonance range for ^{115m}In production at $\sigma_{^{115m}\text{In}} = 0.35$ barn. This determined cross section range corresponds to the mean kinetic energy E_{mean} of the initial neutrons.

VI. ACKNOWLEDGEMENTS

The presented results were obtained in the experiment P176 performed in the framework of FAIR Phase-0 at the PHELIX laser facility at the GSI Helmholtzzentrum für

Schwerionenforschung GmbH in Darmstadt, Germany. We thank the PHELIX team for the support. The research of N.E.A. was supported by The Ministry of Science and Higher Education of the Russian Federation (Agreement with Joint Institute for High Temperatures RAS No 075-15-2020-785 dated September 23, 2020).

VII. AUTHOR CONTRIBUTIONS

M.M.G. was writing the manuscript and conceived the scheme. M.M.G. and P.T. evaluated the results from the nuclear diagnostics. M.M.G., and M.G. performed the illustration of the results. A.S. and A.K. were performing GEANT4 simulations. A.P. and N.E.A. provided theo-

retical support. N.G.B. fabricated the aerogel-foam targets and provided related target information. O.N.R., S.Z. and M.G. evaluated the results from the electron diagnostics and performed illustrations. The experimental studies were performed by M.M.G., O.N.R., P.T., M.G. and S.Z.. All authors discussed the results, commented on the manuscript, and agreed on the contents.

VIII. MATERIALS AND CORRESPONDENCE

The data that support the findings of the present studies are available from the corresponding author (M.M.G.) on request.

-
- [1] Miquel, J-L. & Lion, C. & Vivini, P.. The Laser Mega-Joul: LMJ&PETAL status and Program Overview. *Journal of Physics: Conf. Series* **688**, 012067 (2016).
- [2] Moses, E. I. et al.. Overview: Development of the National Ignition Facility and the Transition to a User Facility for the Ignition Campaign and High Energy Density Scientific Research. *Fusion Science and Technology* **69**, pp. 1-24 (2016).
- [3] Le Pape, S. et al.. X-ray radiography and scattering diagnosis of dense shock-compressed matter. *Physics of Plasmas* **17**, 056309 (2010).
- [4] Morace, A. et al.. Development of x-ray radiography for high energy density physics. *Physics of Plasmas* **21**, 102712 (2014).
- [5] Glenzer, S. H. et al. First implosion experiments with cryogenic thermonuclear fuel on the National Ignition Facility. *Plasma Physics and Controlled Fusion* **54**, 045013 (2012).
- [6] Frenje, J. A. et al. Diagnosing implosion performance at the National Ignition Facility (NIF) by means of neutron spectrometry. *Nuclear Fusion* **53**, 043014 (2013).
- [7] Thirolf, P., and Habs, D. Bright perspectives for nuclear photonics. *The European Physical Journal Special Topics* **223**, 1213–1219 (2014).
- [8] Arai, M., and Crawford, K. Neutron Sources and Facilities. In: Billeux, R., McGreevy, R. & Anderson, I. (eds) Neutron Imaging and Applications: *Neutron Scattering Applications and Technologies* (Springer, Boston, MA, 2009).
- [9] Tanaka, K. A. et al. Current status and highlights of the ELI-NP research program. *Matter and Radiation at Extremes* **5**, 024402 (2020).
- [10] Krasny, M. W. The Gamma Factory proposal for CERN. *Proceedings of Science: EPS-HEP2017*, 532 (2018).
- [11] Habs, D., and Köster, U. Production of Medical Radioisotopes with High Specific Activity in Photonuclear Reactions with γ Beams of High Intensity and Large Brilliance. *Appl. Phys. B* **103**, 501–519 (2011).
- [12] Köster, U., Günther, M. M., and Habs D., Production of radioisotopes with high specific activity by photonuclear reactions: From a “wild idea” to reality. *Radiotherapy and Oncology* **102**, 102–103 (2012).
- [13] Reifarh, R, Lederer, C., and Käppeler, F. Neutron reactions in astrophysics. *Journal of Physics G: Nuclear and Particle Physics* **41**, 053101 (2014).
- [14] Mor, I. et al. Reconstruction of Material Elemental Composition Using Fast Neutron Resonance Radiography. *Physics Procedia* **69**, 304–313 (2015).
- [15] Lan, H.Y. et al.. Determination of the photodisintegration reaction rates involving charged particles: Systematic calculations and proposed measurements based on the facility for Extreme Light Infrastructure–Nuclear Physics. *Physical Review C* **98**, 054601 (2018).
- [16] Luo, W., Bobeica, M., and Gheorghe, I. et al. Estimates for production of radioisotopes of medical interest at Extreme Light Infrastructure – Nuclear Physics facility. *Applied Physics B* **122**, 8 (2016).
- [17] Loveless, C.S. et al. Photonuclear production, chemistry, and in vitro evaluation of the theranostic radionuclide ^{47}Sc . *EJNMMI Research* **9**, 42 (2019).
- [18] Ma, Z. et al.. Photonuclear production of medical isotopes $^{62,64}\text{Cu}$ using intense laser-plasma electron source. *Matter and Radiation at Extremes* **4**, 064401 (2019).
- [19] Pruet, J., McNabb, D., Hagmann, C.A., Hartemann, F.V., and Barty, C. Detecting clandestine material with nuclear resonance fluorescence. *Journal of Applied Physics* **99**, 123102–123102 (2006).
- [20] Altstadt, E. et al.. A photo-neutron source for time-of-flight measurements at the radiation source ELBE. *Annals of Nuclear Energy* **34**, pp. 36–50 (2007).
- [21] Institut Laue-Langevin <http://www.ill.eu> (2020).
- [22] Taylor, A. et al. A Route to the Brightest Possible Neutron Source?. *Science* **315**, pp. 1092–1095 (2007).
- [23] Garoby, R. et al. The European Spallation Source Design. *Physica Scripta* **93**, 014001 (2018).
- [24] Nowicki, S. F., Wender, S. A., & Mocko, M. The Los Alamos Neutron Science Center Spallation Neutron Sources. *Physics Procedia* **90**, pp. 374-380 (2017).
- [25] Alzubaidi, S., Bartz, U., Basten, M. et al.. The Frankfurt neutron source FRANZ. *Eur. Phys. J. Plus* **131**, 124 (2016).
- [26] Thielemann, F.-K. et al. What are the astrophysical sites for the r-process and the production of heavy elements?. *Progress in Particle and Nuclear Physics* **66**, pp. 346 – 353 (2011).

- [27] Horowitz, C. J. et al. r-process nucleosynthesis: connecting rare-isotope beam facilities with the cosmos. *Journal of Physics G: Nuclear and Particle Physics* **46**, 083001 (2019).
- [28] Sonnabend, K. et al. The (n, γ) cross sections of short-living s-process branching points. *AIP Conference Proceedings* **704**, p. 463 (2004).
- [29] Chen, S.N. et al., Extreme brightness laser-based neutron pulses as a pathway for investigating nucleosynthesis in the laboratory. *Matter and Radiation at Extremes* **4**, 054402 (2019).
- [30] Hill, P. and Wu Y.. Exploring laser-driven neutron sources for neutron capture cascades and the production of neutron-rich isotopes. *Physical Review C* **103**, 014602 (2021).
- [31] <https://tunl.duke.edu/research/our-research/beam-physics> (2020).
- [32] Hooker, S. Developments in laser-driven plasma accelerators. *Nature Photonics* **7**, 775–782 (2013).
- [33] Ta Phuoc, K., Corde, S., Thauray, C. et al. All-optical Compton gamma-ray source. *Nature Photonics* **6**, 308–311 (2012).
- [34] Cipiccia, S., Islam, M., Ersfeld, B. et al. Gamma-rays from harmonically resonant betatron oscillations in a plasma wake. *Nature Phys.* **7**, 867–871 (2011).
- [35] Yu, C., Qi, R., Wang, W. et al. Ultrahigh brilliance quasisynchrochromatic MeV γ -rays based on self-synchronized all-optical Compton scattering. *Sci. Rep.* **6**, 29518 (2016).
- [36] Norreys, P. A. et al. Observation of a highly directional γ -ray beam from ultrashort, ultraintense laser pulse interactions with solids. *Physics of Plasmas* **6**, 2150 (1999).
- [37] Palaniyappan, S. et al. MeV bremsstrahlung X rays from intense laser interaction with solid foils. *Laser and Particle Beams* **36**, 502 (2018).
- [38] Giulietti, A. et al. Intense γ -Ray Source in the Giant-Dipole-Resonance Range Driven by 10-TW Laser Pulses. *Physical Review Letters* **101**, 105002 (2008).
- [39] Schumaker, W. et al. Measurements of high-energy radiation generation from laser-wakefield accelerated electron beams. *Physics of Plasmas* **21**, 056704 (2014).
- [40] Ain, Q., Li, S., Mirzaie, M., and Hafz, N. A. M. Generation of GeV Electron Beam From a Laser-Plasma Accelerator and Its Prospect as a Desktop Source of Energetic Positrons and Gamma Rays For Applications. *IEEE Transactions on Nuclear Science* **65**, pp. 2671–2678 (2018).
- [41] Zhu, X.-L. et al. Extremely brilliant GeV γ -rays from a two-stage laser-plasma accelerator. *Sci. Adv.* **6**, eaaz7240 (2020).
- [42] Benedetti, A., Tamburini, M., and Keitel, C. H.. Giant collimated gamma-ray flashes. *Nature Photonics* **12**, 319–323 (2018).
- [43] Zhu, X.-L. et al. Dense GeV electron-positron pairs generated by lasers in near-critical-density plasmas. *Nature Communications* **7**, 13686 (2016).
- [44] Ridgers, C. P. et al. Dense Electron-Positron Plasmas and Ultraintense γ rays from Laser-Irradiated Solids. *Phys. Rev. Lett.* **108**, 165006 (2012).
- [45] Luo, W. et al.. Dense electron-positron plasmas and gamma-ray bursts generation by counter-propagating quantum electrodynamics-strong laser interaction with solid targets. *Physics of Plasmas* **22**, 063112 (2015).
- [46] Roth, M. et al. Bright Laser-Driven Neutron Source Based on the Relativistic Transparency of Solids. *Phys. Rev. Lett.* **110**, 044802 (2013).
- [47] Jung, D. et al. Characterization of a novel, short pulse laser-driven neutron source. *Physics of Plasmas* **20**, 056706 (2013).
- [48] Petrov, G. M. et al. Generation of energetic (>15 MeV) neutron beams from proton- and deuteron-driven nuclear reactions using short pulse lasers. *Plasma Physics and Controlled Fusion* **55**, 105009 (2013).
- [49] Kleinschmidt, A. et al. Intense, directed neutron beams from a laser-driven neutron source at PHELIX. *Physics of Plasmas* **25**, 053101 (2018).
- [50] Pomerantz, I. et al. Ultrashort Pulsed Neutron Source. *Phys. Rev. Lett.* **113**, 184801 (2014).
- [51] Jiao, X.J. et al. A tabletop, ultrashort pulse photoneutron source driven by electrons from laser wakefield acceleration. *Matter and Radiation at Extremes* **2**, pp. 296–302 (2017).
- [52] Willingale L. et al.. The unexpected role of evolving longitudinal electric fields in generating energetic electrons in relativistically transparent plasmas. *New Journal of Physics* **20**, 093024 (2018).
- [53] Rosmej, O. N. et al. Interaction of relativistically intense laser pulses with long-scale near critical plasmas for optimization of laser based sources of MeV electrons and gamma-rays. *New Journal of Physics* **21**, 043044 (2019).
- [54] Rosmej, O. et al. High-current laser-driven beams of relativistic electrons for high energy density research. *Plasma Physics and Controlled Fusion*, (2020).
- [55] Pukhov, A., Sheng, Z.-M., and Meyer-ter-Vehn, J.. Particle acceleration in relativistic laser channels. *Physics of Plasmas* **6**, 2847 (1999).
- [56] Pukhov, A.. Strong field interaction of laser radiation. *Rep. Prog. Phys.* **66**, pp. 47–101 (2003).
- [57] Bagnaud, V. et al. Bagnoud et al. Commissioning and early experiments of the PHELIX facility. *Appl. Phys. B* **100**, 137–150 (2010).
- [58] Borisenko, N. G. et al. Plastic aerogel targets and optical transparency of undercritical microheterogeneous plasma. *Fusion science and technology* **51**, 655–664 (2007).
- [59] Gus'kov S. Yu. et al. Laser-supported ionization wave in under-dense gases and foams. *Physics of Plasmas* **18**, 103114 (2011).
- [60] Pugachev, L. P. et al.. Acceleration of electrons under the action of petawatt-class laser pulses onto foam targets. *Nuclear Instruments and Methods in Physics Research A* **829**, pp. 88–93 (2016).
- [61] Pugachev, L. P., and Andreev, N. E. Characterization of accelerated electrons generated in foams under the action of petawatt lasers. *Journal of Physics: Conference Series* **1147**, 012080 (2019).
- [62] Günther, M. M. et al. A novel nuclear pyrometry for the characterization of high-energy bremsstrahlung and electrons produced in relativistic laser-plasma interactions. *Physics of Plasmas* **18**, 083102 (2011).
- [63] Agostinelli, S. et al. GEANT4-a simulation toolkit. *Nuclear Instruments and Methods in Physics Research Section A Accelerators Spectrometers Detectors and Associated Equipment* **506**, 250 (2003).
- [64] Bonnet, T. et al. Response functions of imaging plates to photons, electrons and ^4He particles. *Review of Scientific Instruments* **84**, 103510 (2013).
- [65] Huang, T. W. et al.. Highly efficient laser-driven Compton gamma-ray source. *New Journal of Physics* **21**,

- 013008 (2019).
- [66] Pukhov, A., Three-dimensional electromagnetic relativistic particle-in-cell code VLPL (Virtual Laser Plasma Lab). *Journal of Plasma Physics* **61**, 425–433 (1999).
- [67] Borghesi, M., Laser-driven ion acceleration: State of the art and emerging mechanisms. *Nuclear Instruments and Methods in Physics Research Section A: Accelerators, Spectrometers, Detectors and Associated Equipment* **740**, 6–9 (2014).
- [68] Robson, L., Simpson, P., Clarke, R. et al. Scaling of proton acceleration driven by petawatt-laser-plasma interactions. *Nature Phys.* **3**, 58–62 (2007).
- [69] Sgattoni, A. et al.. Laser ion acceleration using a solid target coupled with a low-density layer. *Physical Review E* **85**, 036405 (2012).
- [70] Bin, J.H. et al., Enhanced Laser-Driven Ion Acceleration by Superponderomotive Electrons Generated from Near-Critical-Density Plasma. *Physica Review Letters* **120**, 074801 (2018).
- [71] Ma, W. J. et al.. Laser Acceleration of Highly Energetic Carbon Ions Using a Double-Layer Target Composed of Slightly Underdense Plasma and Ultrathin Foil. *Physical Review Letter* **122**, 014803 (2019).
- [72] Willingale, L. et al.. High-power, kilojoule laser interactions with near-critical density plasma. *Physics of Plasmas* **18**, 056706 (2011).
- [73] Zankl, G., Strachan, J.D., Lewis, R., Pettus, W., and Schmotzer, J. Neutron flux measurements around the Princeton large tokamak. *Nuclear Instruments and Methods in Physics Research* **185**, 321–329 (1981).
- [74] Bertulani, C. A. Nuclear Reactions (Wiley-VCH, Berlin, 2009).
- [75] <http://www-nds.iaea.org/exfor>
- [76] Günther, M. M. et al. Dispersive refraction of different light to heavy materials at MeV γ -ray energies. *Physical Review A* **97**, 063843 (2018).
- [77] Burbidge, E. M., Burbidge, G. R., Fowler, W. A., and Hoyle, F. Synthesis of the Elements in Stars. *Rev. Mod. Phys.* **29**, 547 (1957).
- [78] Cowan, J. J., Cameron, A. G. W., and Truran, J. W. R-process nucleosynthesis in dynamic helium-burning environments. *The Astrophysical Journal* **294**, 656 (1985).
- [79] Lederer, C. et al. Experiments with neutron beams for the astrophysical s process. *Journal of Physics: Conference Series* **665**, 012020 (2016).
- [80] Ji, A. P. et al. R-process enrichment from a single event in an ancient dwarf galaxy. *Nature* **531**, p. 610 (2016).
- [81] Tanaka, K. A. et al. Calibration of imaging plate for high energy electron spectrometer. *Review of Scientific Instruments* **76**, 013507 (2005).
- [82] Rusby D. R. et al. Measurement of the angle, temperature and flux of fast electrons emitted from intense laser-solid interactions. *Journal of Plasma Physics* **81**, 475810505 (2015).
- [83] Koning, A.J., and Rochman, D. Modern Nuclear Data Evaluation with the TALYS Code System. *Nuclear Data Sheets* **113**, Issue 12, 2841-2934 (2012).